An acoustic emission analysis of glass-ceramic sealants for solid oxide fuel and electrolysis cells exposed to torsional tests: room and high-temperature experiments

V.H. Rangel-Hernandez, Q. Fang, J. Malzbender, Markus G. R. Sause, C. Babelot, S.M. Gross-Barsnick, L. Blum

Rangel-Hernandez, V.H., Q. Fang, J. Malzbender, Markus G. R. Sause, C. Babelot, S.M. Gross-Barsnick, and L. Blum. 2021. "An acoustic emission analysis of glass-ceramic sealants for solid oxide fuel and electrolysis cells exposed to torsional tests: room and high-temperature experiments." *International Journal of Hydrogen Energy* 46 (27): 14724–34. https://doi.org/10.1016/j.ijhydene.2021.01.232.

An acoustic emission analysis of glass-ceramic sealants for solid oxide fuel and electrolysis cells exposed to torsional tests: Room and high-temperature experiments

V.H. Rangel-Hernandez [a,*], Q. Fang [a], J. Malzbender [a], M.G.R. Sause [b], C. Babelot [c], S.M. Gross-Barsnick [c], L. Blum [a]

[a] Forschungszentrum Jülich GmbH, Institute of Energy and Climate Research (IEK), 52428, Jülich, Germany
[b] University of Augsburg, Institute for Physics, Experimental Physics II, D-86135, Augsburg, Germany
[c] Forschungszentrum Jülich GmbH, Central Institute for Engineering, Electronics and Analytics (ZEA), Engineering and Technology (ZEA-1), 52428, Jülich, Germany

ABSTRACT

The mechanical integrity of the sealant material is of key importance for the long-term, reliable operation of solid oxide fuel/electrolysis cell stacks. However, *in-situ* monitoring and detection of potential failures in sealing materials using classical electrochemical characterization techniques are difficult tasks. Therefore, in this work, the acoustic emission (AE) technique is applied to monitor and characterize the failure process of a glass-ceramic sealant exposed to torsional shear strength at both room and typical stack operation temperature (750 °C). Hourglass-shaped steel specimens are produced for the tests. A glass-ceramic material with two different porosities is used to join the specimens. The failure process is characterized in terms of AE peak amplitude, AE cumulative hits and AE energy, as well as the average frequency content of the signals. The results indicate that the degree of microscopic damage can be determined from the analysis of the AE energy and the fracture mechanisms can be found by statistical analysis of the average frequency of the signals. The fractured surfaces are visualized by optical microscopy to unveil that specimens with high porosity showed a fully cohesive fracture pattern, while specimens with low porosity showed a partially fracture pattern. As a result, AE method promises to be a potential in-operando technique for monitoring mechanical failure processes inside solid oxide cell stacks.

Keywords:
Acoustic emission
Glass ceramic sealant
Torsion test
Solid oxide cells
Failure
Frequency spectrum

---

* *Corresponding author.*
E-mail address: vrangel@ugto.mx (V.H. Rangel-Hernandez).

Introduction

Both solid oxide fuel cell (SOFC) and solid oxide electrolysis cell (SOEC) technologies have been gaining unprecedented momentum worldwide for low- or zero-emission mobile and power generation/conversion applications, and also as a result of their technical performance. On the one hand, SOFCs feature high electrical efficiency and offer good flexibility, as they can run on either natural gas, coal gas, biogas or hydrogen [1]. On the other hand, SOECs achieve high hydrogen (and syngas via the electrolysis of CO_2 and steam) production efficiency through the use of thermal energy, which significantly decreases demand for electrical energy [2]. However, both technologies are prone to thermo-mechanical degradation due to high operating temperatures and thermal cycling. In this context, one of the components that receives the most attention is the glass-ceramic sealant used to stack the cells and metallic plates, as well as to prevent the leakage of gases among them, and electrical insulation [3].

The special interest of the glass-ceramic sealant derives from the fact that it must withstand the stresses generated by mechanical loads and by the differences in the physical and mechanical properties (e.g., thermal expansion coefficients, melting points, etc.) of the different materials [4–6]. All of this is due to the harsh conditions to which they are subjected. However, monitoring of mechanical integrity and timely detection of potential failure mechanisms in sealant materials and ceramic cells has not been possible until now using current electrochemical characterization techniques [7–9].

As a result, glass-ceramic sealant materials are the focus of much research, with a particular emphasis on their thermomechanical optimization and improvement [10–12]. In the case of the development of novel glass-ceramic sealants and the improvement of existing ones, the Forschungszentrum Jülich in Germany, together with external partners has to date made important contributions in the area of fracture analysis [13], modeling by means of finite analysis [14], as well as the improvement of the thermomechanical properties of sealants by reinforcing them with other materials [15] or altering their preparation [16].

At the same time, the current literature contains important contributions towards, on the one hand, the development of new sealing materials that satisfy the thermomechanical and thermochemical compatibility between the different materials [17–20]. Moreover, novel sealants are being produced through the addition of components such as glass fibers as a reinforcement material, which promise to achieve highly tight gas sealants for high-temperature use [21], or the inclusion of alkaline metals in order to obtain sealants with long-term thermal stability [22]. Under real operating conditions, the sealant is primarily subjected to tension and shear stresses that can result in its failure [5,23]. For this reason, thermomechanical characterization also plays an important role in understanding the behavior of sealants at the operating temperatures of stacks. To date, these have mostly comprised tension [24–26] and bending tests [13,27]; in contrast, torsion tests, although considered the most suitable for evaluating shear [28], have been very limited, especially at the actual operating temperatures of SOFC/SOEC stacks. Torsion tests are of particular interest, because they enable the evaluation and comparison of the shear stresses yielded by different configurations, which are specially prepared with glass-ceramic sealants, and tested at room- and high temperatures [29–31]. These results, combined with mathematical computer models, provide a better comprehension of the stress distribution in the sealant and other components [5,32]. It has also been shown that thermal aging induced in a glass-ceramic material may cause a considerable increase in creep resistance but, in turn, a reduction in crack healing capacity [33]. The characterization of the chemical and mechanical behavior of the interface between the glass-ceramic sealant and metal interconnections should also be addressed, as the formation of coating layers, due to the interaction between them, can be detrimental to the system's integrity over time [34–36].

However, despite advances in the techniques for evaluating the thermomechanical aspects of solid oxide fuel/electrolysis cells [37,38], a few investigations have been performed in which the technique of acoustic emission (AE) has been used in accordance with the works mentioned above. The AE technique is a recognized test among the different non-destructive methods commonly used to detect and locate mechanical failures in metallic, non-metallic, and composites structures and components under load [39–41]. It is noteworthy that the AE signals generated during any monitoring are generally stochastic in nature, and therefore statistical methods are commonly utilized in their interpretation [42,43].

In the specific case of glass-ceramic materials, the AE technique has been used to understand and identify typical sources of the fracture mechanisms in these materials [44–46]. The implementation of this technique during tensile tests, on these types of materials has demonstrated the discrimination of fracture mechanisms such as matrix cracking, delamination, debonding and fiber breaking [24,47,48]. The utility of the AE technique in torsion tests, on the contrary, has been more limited, in particular those performed at stack operating temperatures [49–51]. It seems that, up until now, the AE method has rarely been applied to the study of the effect of porosity on the failure behavior of glass-ceramic sealants.

In view of the above, and as far as the authors are aware, there is still a need to better understand the fracture process of glass-ceramic sealants under torsional strengths and at stack operating temperatures, especially when its level of porosity varies. Therefore, this investigation presents the application of the AE technique to the monitoring and characterization of the failure process of glass ceramic sealant specimens; featuring low and high porosity, and exposed to torsion strength at both room and typical stack operating temperatures. The comparison is based on the analysis of AE signal features, namely the amplitude, AE cumulative hits, and AE energy, as well as the average frequency content of the signals. Finally, in order to support the analysis, the fractured surfaces are examined by means of optical microscopy.

Experimental

Specimen preparation

The glass-ceramic composite sealant used in the current work is comprised of a glass matrix of the system BaO–CaO–SiO_2 named "H" reinforced with 13 wt.-% yttrium-stabilized-zirconium oxide (YSZ) fibers [14]. The chemical composition of glass H was analyzed by inductively coupled plasma optical emission spectroscopy (ICP-OES) after alkaline pulping to be 48.2 wt.-% for BaO, 6.1% for CaO and 29.8% for SiO_2 balanced by additions of Al_2O_3, B_2O_3, V_2O_5 and ZnO. The composite sealant of glass H with fibers has a coefficient of thermal expansion of $9.3 \times 10^{-6}\ K^{-1}$ [52]. Further details on the preparation and chemical composition of glass H are provided in Refs. [14,53]. The crystallization behavior of the glass matrix is investigated in Ref. [54] and the viscous flowing of composites are explained in Ref. [55]. For the type of tests carried out in the current work, hourglass-shaped specimens were used as previously considered in Ref. [31], in particular, the successfully developed hollow-full specimen configuration with annulus shape sealant [15,30,56]. Crofer22H steel was used in the manufacture of the specimens. An approximately 0.5 mm-thick layer of screen-printed sealant was deposited on one side of the two halves of the Crofer22H, resulting in final specimens as illustrated in Fig. 1.

The application of the glass-ceramic sealant was performed by two different organic paste formulations, one of which caused greater porosity in the specimen after joining. The screen printing technique was used on an intermediate carrier foil to obtain green seal gaskets from which the circular seals were obtained by stamping. A screen printer ESC AT 60 PD of Europa Siebdruckmaschinen Centrum GmbH&Co.KG was used with polyester screens 8–300 produced by Koenen GmbH of 560 μm thickness, a mesh width of 950 μm and bottom coating of 350 μm. One of the paste formulations was based on a butylglycolate binder as described in Ref. [57], while in the other formulation α-terpineole was used as a solvent instead of the butylglycolate.

It is important to mention that on some occasions the binder containing butylglycolate yielded a foam-like porosity in the joint, while the terpineole-based media always generated a dense sealing material. The reason why porosity was yielded is not yet fully understood. A possible explanation is that a decomposition of the butylglycolate took place resulting in the formation of hardly combustible organic compounds. These species could give rise to an excess of active carbon in the glass, which burns at temperatures above the viscous flow of the glass, thus forming the foam-like structure. The joining of the specimens was carried out in a jig that allows a precise centering of the two halves of the samples and applies a dead load of 4 kg on top. The thermal treatment for the joining of the specimens consisted in heating them, by means of air, at a rate of 2 K/min up to 350 °C and 550 °C with a dwelling of 60 min each so as to achieve the binder burnout. The joining was then carried out at 850 °C for 100 h.

In accordance with the above, and for the issue of monitoring the fracture mechanism of the material under torsional strength, two low porosity and two high porosity specimens were prepared. The terms high and low used here correspond to a percentage range of porosity, so high corresponds to a range of 16–19%; whereas for low, the range is from 1.4 to 2.2%.

AE equipment and parameters

The commercial equipment used in this investigation was an AMSYS-6 from Vallen Systeme GmbH [58]. It included four wideband AE sensors (VS160-NS) with a frequency range from 100 to 450 kHz as well as AE preamplifiers (AEP5H) with a gain of 34 dB at 50 Ω. Table 1 summarizes the acquisition parameters set in the AE equipment.

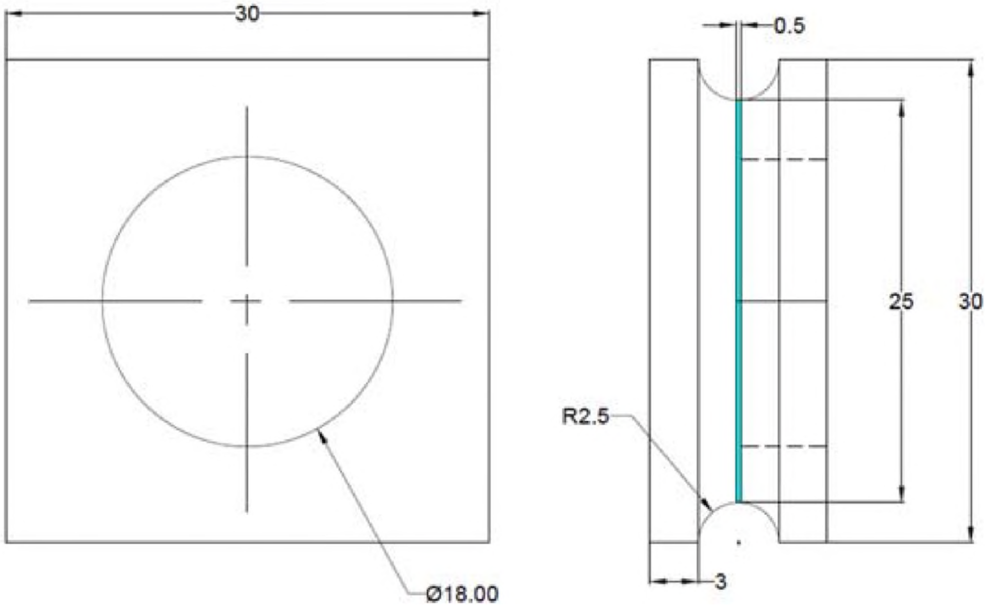

Fig. 1 – Illustration of the prepared hollow-full specimens. Dimensions are in mm.

Experimental installation and testing procedure

Torsion tests were performed on a testing rig on which the specimens used here could be mounted [31,56]. The installation consists of the torque test bench fitted with a furnace in order to be able to carry out the tests at high temperature, with the AE sensors mounted and fixed to the solid cylindrical tubes by means of clamps, as well as the AE acquisition system. Vacuum grease was used as the coupling agent to improve the sensing response. A pencil-lead break test was then used to verify the correct setting up of the AE sensors [59]. An illustration of the torsion test set-up is shown in Fig. 2.

With respect to the procedure for the torsion tests, the specimens were gradually twisted until fracture occurred at a rate of approximately 4°min^{-1}. Table 2 identifies the specimens according to the type of test and porosity level.

Vallen [58] and Origin [60] software were used to perform the real time data recording and post-data processing. Finally, the fractured surfaces were visualized by optical microscopy in order to make a correlation between the cracks observed in the fractured surfaces and the recorded data.

Results and discussion

AE activity

Fig. 3 displays a comparison of the evolution of the torsion load (red line) and the AE peak amplitude of the acoustic emission activity during the torsion testing of a glass-ceramic sealant with high and low porosity at room (a) and high temperature (750 °C) (b) as a function of time. There is a clear variation in the emission patterns in each of the tests.

In the case of the tests at room temperature represented in Fig. 3 (a), the torque until failure for the high-porosity specimen (maximum torque 95 Nm) was 54% lower than for the low-porosity specimen. The high porosity in the material lead to a low shear strength. A possible explanation for this is that the higher the number of pores in the material, the smaller the bonding surface between either the inner layers of the sealant or the sealant-steel interface, and so less torque was required for fracturing. This is consistent with previous studies where this phenomenon has also been addressed [61]. Thus, the number of acoustic emissions of the high-porosity specimens is higher than that of the low-porosity ones. Acoustic emission activity is higher near the end of the test in high-porosity specimen. The contrary is true for low-porosity specimens. This difference could be due to two reasons. On the one hand, there is a high speed of crack propagation in the high-porosity specimen due to its low tortuosity, which could lead to low fracture energy as previously reported in Ref. [62]. On the other hand, it is possible that the greater number of small areas among the pores fail before the specimen reaches failure. At a very high AE amplitude, there is a correlation between the AE amplitude and torque occurring due to macroscopic failure at the end.

Table 1 – Acquisition parameter of the AE equipment.

AE data sample rate	10 MHz
TR data sample rate	5 MHz
Threshold	40 dB
Pre-trigger samples	200 µs
Preamplifier gain	34 dB
Digital filter	95 kHz–850 kHz

With respect to the torsion tests at 750 °C, the evolution of acoustic events arising during the application of the torque is presented in Fig. 3(b). The torque curve revealed by the low-porosity specimen reveals a remarkable elastic-plastic behavior, from which it can be inferred that the plasticity of the material increased at high temperature due to the residual glass phase of the composite. However, the shear stress decreased by about 20% in the case of the high-porosity specimen and 35% in the case of the low-porosity one. Furthermore, in both cases, there is remarkable acoustic emission activity immediately after the onset of the test, within the amplitude range of 70–100 dB. This finding might be an indication that at the beginning of the test micro-mechanical stresses redistribute within the glass-ceramic material, i.e., extensive micro-cracking is present. In porous material, stresses primarily concentrate around defects or pores until saturation. Then, the crack might start in one of these and propagate through the material in the case of the low-porosity specimen, the crack will propagate more slowly due to the high tortuosity of the material. However, after saturation, the AE activity decreased in the non-linear range or plastic zone. This finding might suggest that, within the plastic zone, the phase transformation generates a few micro-cracks and therefore a low number of acoustic emissions. A similar behavior was observed in a recent study, where ceria-stabilized zirconia-based ceramics showed nearly zero extensive micro cracking in the plastic region [63].

AE cumulative hits and energy

Fig. 4 reveals the correlation between the cumulative AE hits and torque for glass-ceramic sealant specimens featuring low porosity (a) and high porosity (b) tested at room and high temperature. The initial values from zero up to point a and point a’ (see Fig. 4) are not considered, as they mainly derive from the influence of initial AE bursts due to system adjustment.

In the case of the low-porosity specimen (see Fig. 4(a)), the rate of cumulative AE hits is faster with increasing temperature. At room temperature, as the external torque increases, the rate of damage to the glass-ceramic material rises slowly up to 150 Nm (point b’). From this slope change the rate of cumulative AE hits grows uncontrolled until failure at 170 Nm (point c’). For the high-temperature test, the cumulative AE hits increases rapidly until the point of change of the slope (point b), at approximately 97% of the maximum torque, from where the AE hits triggers until the failure of the specimen (point c).

For the high-porosity specimen, the rate of cumulative AE hits increases as the temperature decreases (see Fig. 4(b)). At room temperature, the rate of cumulative AE hits increases slowly to the slope change point (point b’), which corresponds to roughly 50% of the maximum torque. Then, it begins a zone of uncontrolled cumulative AE hits as the torque loading continues until the point of failure (point c’) at 95 Nm. This

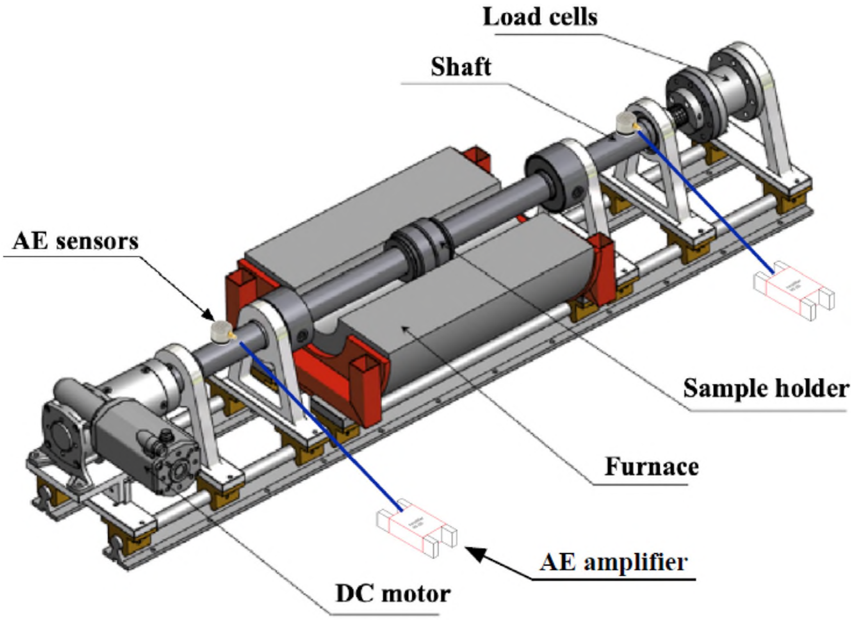

Fig. 2 – Torsion test set-up.

Table 2 – Identification of specimens by porosity and test temperature.

Specimen	Porosity level	Test temperature
FZ-01	High: 16–19%	Room
FZ-02	Low: 1,4–2,2%	Room
FZ-03	High: 16–19%	750 °C
FZ-04	Low: 1,4–2,2%	750 °C

zone corresponds to the high activity of acoustic emission located in Fig. 3(a), which was previously provided for the case of the high-porosity specimen. This implies that the higher the acoustic emission activity, the higher the number of cumulative AE hits. At a high temperature (e.g., 750 °C), the rate of cumulative AE hits grows practically linear until failure at 80 Nm (point b). In this particular case, there is no change in the slope of the curve, as seen in the other curves.

From the comparison of both specimens at room temperature, it is seeming that the rate of damage present in the high-porosity specimen is faster than that in the low-porosity one, but this is only true from a torque force of 50 Nm (between points b' and c'). This result may have two main causes. The first is that this finding could be due to the formation of small cracks at times with only short crack growth distances. The second derives from the fact that increasing the porosity reduces the cross-section of the material and therefore increases its brittleness, although this may also be due to the distribution of the pores and increases the local stress.

However, in the case of the tests at 750 °C, the rate of cumulative AE hits was very similar between the two specimens. Nevertheless, the patterns of the curves differ. In the case of the low-porosity specimen the shape of the curve may be due to the diversity in the size of the cracks. While in the case of the high-porosity specimen, the shape of the curve could be due to the continuous distribution of crack sizes.

As mentioned above, the application of the torsional load to the specimens triggered the onset of micro cracks, which in turn released transient energy that propagated through the specimen and was recorded in the AE sensors. Such energy can be identified as AE energy and is visualized as a function of the torque load in Fig. 5. For the low-porosity specimen, Fig. 5(a), at room temperature, it can be noticed that during the initial application of the torque load the AE energy increased sharply (point a'), then grew linearly until the point of significant change or "knee" at 160 Nm was reached (point c'). The knee is a key indicator of the onset of failure [64], wherein the AE energy reaches its peak (170 Nm).

At high temperature, however, the cumulative AE energy showed an appreciable difference as a result of the torque load. During the initial stage, the AE energy suddenly increased until the torque load reached approximately 8.5% of its ultimate load, as is shown in Fig. 5(a) (point b). As the increase in the torsion load continues, the curve becomes non-linear, i.e. plastic behavior, until its failure as depicted in Fig. 5(a) (point c).

Referring now to the high-porosity specimen, the curve corresponding to the room temperature test shows several important changes in the slope. In the initial stage of torque application, the AE energy increases linearly up to the knee located at 10% of the ultimate torque load, which means that micro-cracking started in the glass ceramic sealant. Then, the torque load continues up to 50% of the total torque (Fig. 5 (b) point b') and the AE energy shows a quasi-constant linear growth, from which it can be inferred that micro-cracking ceased because of the saturation of pores and flaws in the material. Then, the AE energy increases linearly prior to reaching the second knee (point c') which indicates the failure of the glass ceramic sealant (point d') as shown in Fig. 5(b).

In the high-temperature test, the AE energy curve revealed that the first signs of micro-cracking started immediately

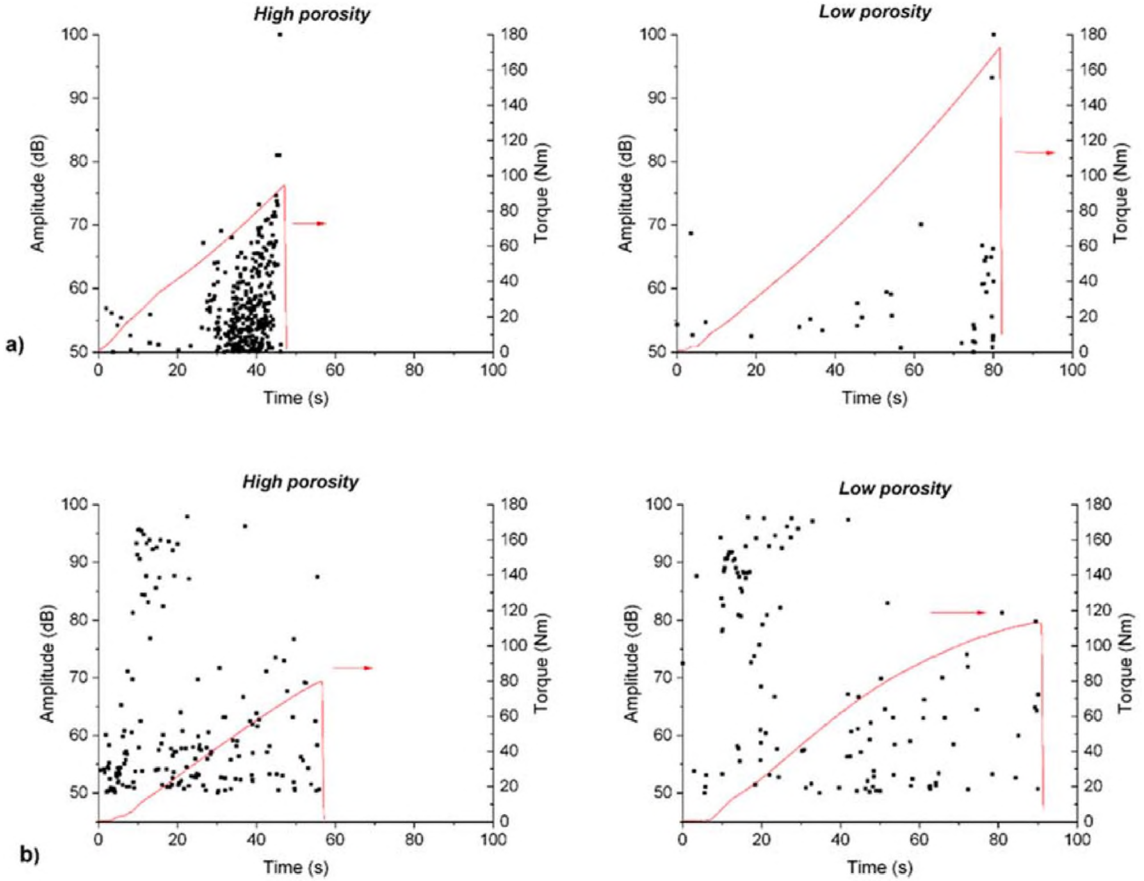

Fig. 3 – AE peak amplitude and torque loading as a function of time for high and low porosity specimens at a) room temperature and b) high temperature, 750 °C.

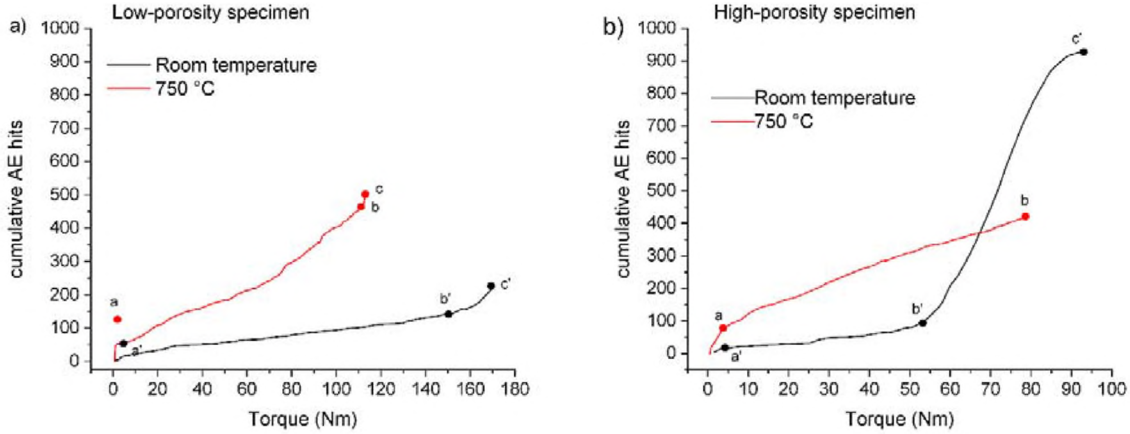

Fig. 4 – Cumulative AE hits as a function of the torque in tests performed on a) low-porosity specimens and b) high-porosity specimens at room and high temperature.

when torque load was applied. In this initial stage, the cumulative AE energy was linear and rapid (point a) and, when reaching approximately 19% of the maximum torque load, a significant change in the slope was observed (point b) (see Fig. 5(b)). After that, the AE energy increased linearly as the torque load continued to be applied until maximum torque was reached at 80 Nm. This is an indication that microcracking spread quickly through the glass-ceramic sealant until failure of the material occurred. This behavior did not appear to give rise to a pore saturation zone, as was seen in the room temperature test.

From this finding it may be inferred that ultimately, the failure of the glass-ceramic sealant is more brittle overall, as only a few large cracks stored the energy and suddenly

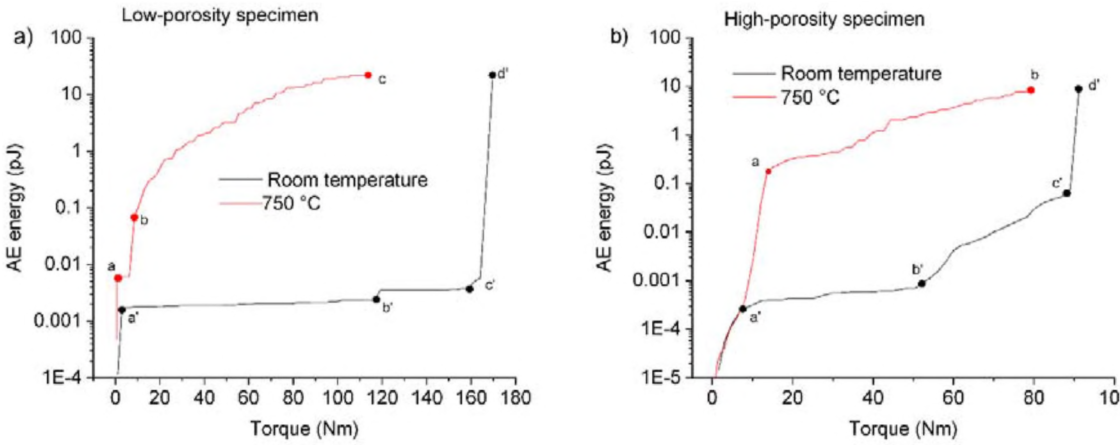

Fig. 5 – AE energy as a function of torque in tests performed on a) low-porosity specimens and b) high-porosity specimens at room and high temperature.

released it at the failure point In the case of the high-porosity specimen, the contact surface of the material decreases, which induces the appearance of smaller cracks as torque is applied, and therefore less energy is stored and released at the end of the test.

Fast Fourier Transform analysis

The cumulative AE hits and energy analysis have revealed consistent indications of the observable micro-cracks. Therefore, in view of classifying the possible failure mechanisms present in the micro-cracks, the average frequency peaks of the signals obtained through the application of the Fast Fourier Transform (FFT) are analyzed. The literature review provides the reported peak frequencies of various failure mechanisms for glass composites such as: matrix cracking (80–250 kHz), fiber/matrix debonding (250–350 kHz) and fiber breakage (350–480 kHz) [65–68].

In each of the tests, as is shown in Fig. 6, the frequency bands are visibly defined: f_1 between 0 and 100 kHz, f_{II} between 100 and 200 kHz, f_{III} between 200 and 300 kHz, f_{IV} between 300 and 400 kHz and, finally, f_V above 400 kHz. For each test, the average frequency (black line) and their corresponding standard deviation (red line) can be observed. At room temperature (Fig. 6(a)), the difference in magnitude of the relative frequencies of the low-porosity specimens by comparison to the high-porosity specimens is evident. In comparison, the difference between the frequency peaks of both specimens is about 6500 mV. Moreover, the frequency analysis reveals that most of the frequency peaks are concentrated within the f_{1I} frequency band. This may suggest the possible identification of the matrix-cracking mechanism. For the frequency bands f_{III}, f_{IV} and f_V, very low frequency magnitudes are found so that none of them is significant enough to enable the distinction of a particular fracture mechanism.

At high temperature (Fig. 6(b)), the difference in the magnitudes of the relative frequencies between the high and low porosity specimens is very large. In the case of the low-porosity specimen, there are two frequency peaks: the first at 100 kHz and the second at approximately 170 kHz within the f_{II} frequency band. The latter coincides with the frequency peak in the high porosity specimen, 170 kHz. As before, this finding may suggest the identification of the matrix-cracking mechanism. The frequencies in the frequency bands f_{III}, f_{IV} and f_V are very low in magnitude, and therefore it is not possible to make a clear distinction over any other fracture mechanism.

The identification of the fracture mechanism presented above is based on the defined average frequency and frequency bands. It is revealed that the frequency band f_{II} is common to all the tests. It is in this band that the highest frequency peaks occurred. Therefore, f_{II} could be associated with matrix cracking. In the case of the other frequency bands, a fracture mechanism could not be identified, as the magnitudes are very low. This is likely that due to the relative position of the damage to that of the AE sensors.

Post-test analysis

In order to gain a better understanding of the fracture process in the specimens measured at room temperature and 750 °C, they were macroscopically inspected after testing. The fracture patterns for room temperature and 750 °C were similar for each type of samples, the images for the torsion test samples at 750 °C are shown in Fig. 7. A fully cohesive fracture pattern is observed for the high-porosity specimens (Fig. 7(a) upper image) with a thicker glass layer on the sample part shown on the left side, visible from the brighter white contrast of the remaining glass ring. The higher magnification of the optical microscopic image (Fig. 7(a) lower image) shows circular pores with a size distribution between a few microns up to 100 μm in diameter. The low-porosity torsion test specimens shows a partially adhesive fracture pattern. About a third of the sample is cohesively broken in the middle of the glass layer (white ring area on the left and right side of Fig. 7(b) upper image). The adhesive fracture pattern shows a brownish-greyish discoloration which is caused by the disruption of oxide scale of the steel. During the joining in air, Crofer22H forms a chromium manganese spinel layer, which is partially dissolved by the glass sealant in a 1–2 μm thin reaction layer. Fig. 7(b) lower image shows part of cohesive

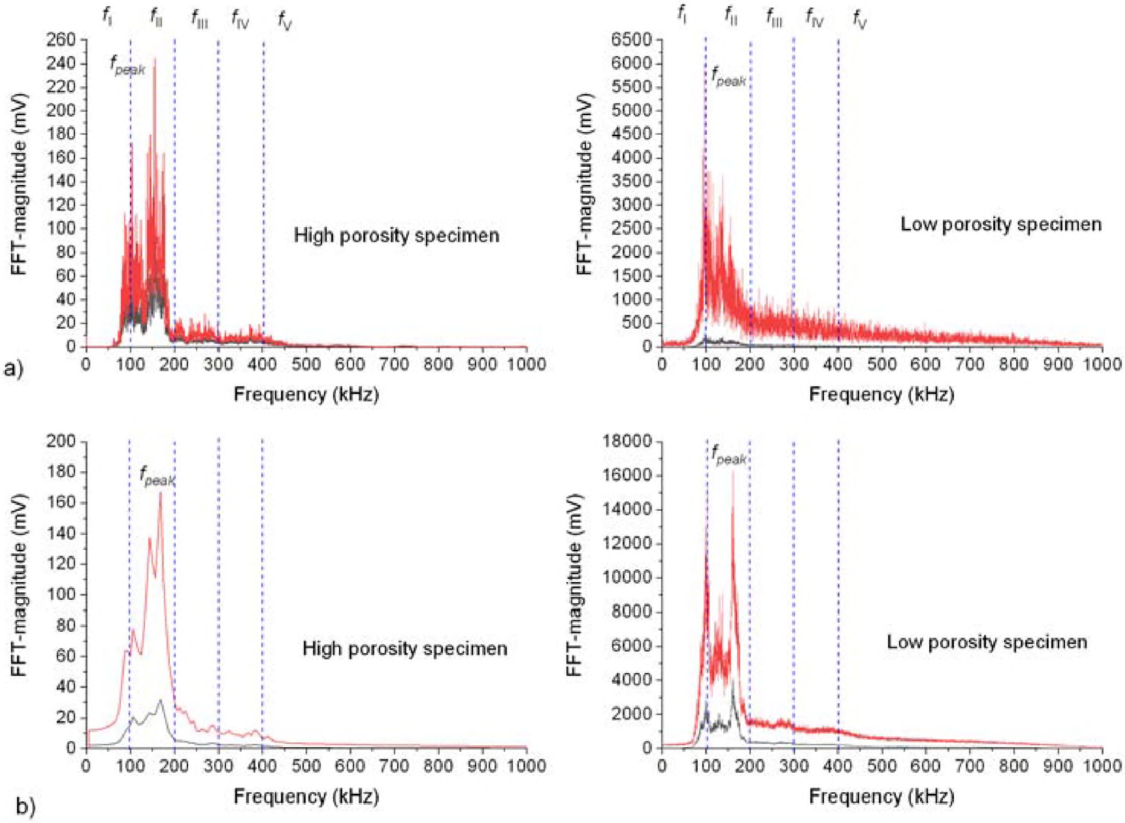

Fig. 6 — Average frequency content of signals recorded during monitoring of the torsion tests at a) room temperature and b) 750 °C for high- and low-porosity specimens.

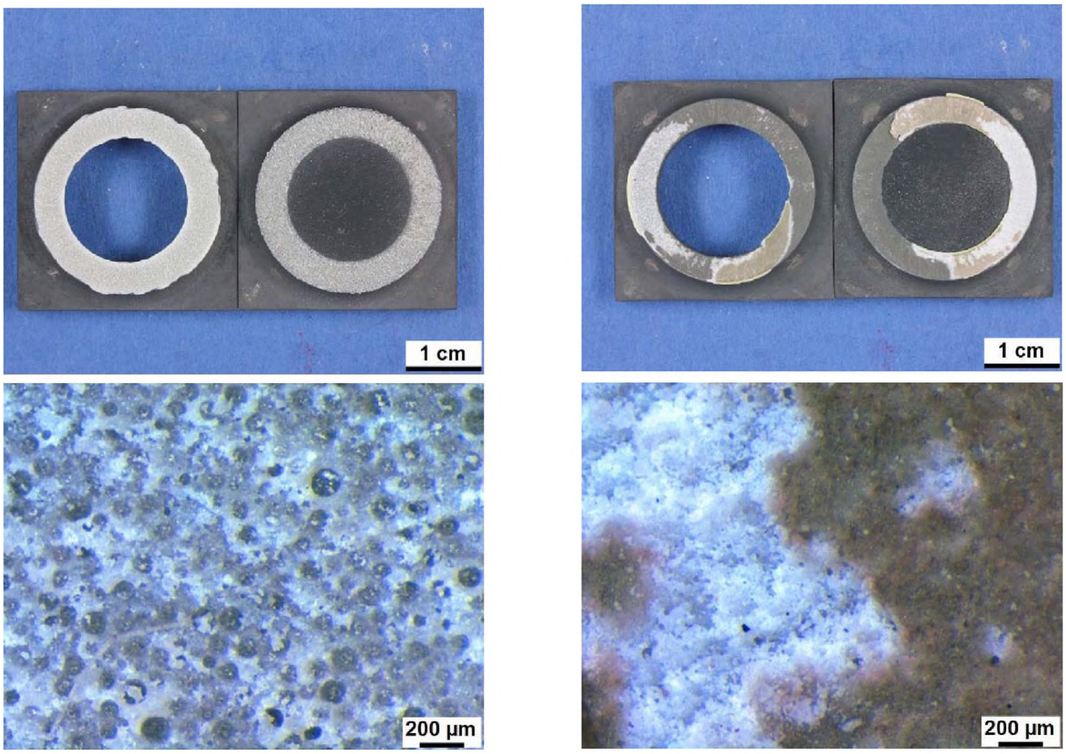

a

b

Fig. 7 — Photographs (upper images) and optical microscope images of the fracture surfaces for a) high- and b) low-porosity glass-ceramic specimens subjected to torsional test at 750 °C.

and part of adhesive fracture of the glass. When regarding the bright area of cohesive fracture, very small pores of about 1–5 μm scale are visible in the glass-ceramic. It is discussable if the reaction zone at the spinel layer of the steel failed under the torsional load or whether the crack was initiated in the middle of the glass-ceramic by a defect and propagated close to the steel surface.

Conclusions

In this study, the fracture process of specimens prepared with low- and high-porosity glass-ceramic sealants loaded in torsion at room and high temperature was monitored using the AE technique. Overall, the results revealed that the acoustic emission patterns of samples with different levels of porosity differed from each other in terms of acoustic activity, AE cumulative hits and AE energy. However, the analysis of the AE cumulative hits did not reveal a clear conclusion of the relationship between these and the fracture mechanisms of the material.

The analysis of the AE energy indicated that in the case of the high porosity specimens the micro-cracks propagated through the ceramic material faster than in low porosity specimens.

It was possible to detect the increase in the plasticity of the matrix as the temperature increased, which exerted a greater effect on the low-porosity specimen. Most importantly, all of these differences in the AE activity could be correlated with good approximation. Only the analysis of the average frequency of the signals allowed the identification of the matrix cracking between a range of 100 and 200 kHz. According to this, it is concluded that the feasibility of the acoustic emission technique for in-situ monitoring of solid oxide cell stacks is promising as long as there is an effective calibration of the AE equipments as well as an adequate statistical analysis to distinguish those signals that contain information on fracture mechanisms from unwanted signals.

Finally, the experimental work at high temperature led to some unanswered questions such as the location of the point where the cracks began, the bonding strength at the interface between the metallic material and the sealant, as well as identifying a correlation between the AE characteristics and the frequency of the signals. Therefore, further tests will be carried out later in order to make a statistical analysis of the application of the acoustic emission technique in the monitoring of glass-ceramic sealant at high temperature under torsion.

Declaration of competing interest

The authors declare that they have no known competing financial interests or personal relationships that could have appeared to influence the work reported in this paper.

The authors declare the following financial interests/personal relationships which may be considered as potential competing interests:

Acknowledgements

The authors would like to express their gratitude for the contribution of colleagues from the different institutes of the Forschungszentrum Jülich, who provided valuable ideas, knowledge and information in the completion of this project. Special thanks to D. Federmann (ZEA-1), M. Fischer (ZEA-1), A. Cramer (ZEA-1) and M. Turiaux (IEK-2). Finally, many thanks to the University of Guanajuato for the sabbatical stay granted during the period 2019–2020.

REFERENCES

[1] Dicks AL, Rand DAJ. Fuel cell systems explained. 3rd ed. New Jersey: Wiley; 2018.
[2] Monzón H, Laguna-Bercero MA. CO2 and steam electrolysis using a microtubular solid oxide cell. J. Phys. Energy 2020;2:014005. https://doi.org/10.1088/2515-7655/ab4250.
[3] Kendall K, Kendall M. High temperature solid oxide fuel cells for the 21st century: fundamentals, design and applications. Oxford: Academic Press; 2016.
[4] Mahapatra MK, Lu K. Glass-based seals for solid oxide fuel and electrolizer cells – a review. Mat Sci Eng R 2010;67:65–85. https://doi.org/10.1016/j.mser.2009.12.002.
[5] Blum L, Groß SM, Malzbender J, Pabst U, Peksen M, Peters R, Vinke IC. Investigation of solid oxide fuel cell sealing behavior under stack relevant conditions at Forschungszentrum Jülich. J Power Sources 2011;196:7175–81. https://doi.org/10.1016/j.jpowsour.2019.09.041.
[6] Wei J. Mechanical characterization of solid oxide fuel cells and sealants. Forschungszentrum Jülich 2016;391. ISBN: 978-3-95806-266-5.
[7] Subotic V, Pofahl S, Lawlor V, Menzler NH, Thaller T, Hochenauer C. Online monitoring tools for SoH diagnostic and prognostic of remaining lifetime of reversible solid oxide cell (rSOC) systems. Energy Procedia 2019;158:2329–34. https://doi.org/10.1016/j.egypro.2019.01.271.
[8] Subotic V, Stoeckl B, Lawlor V, Strasser J, Schroettner H, Hochenauer C. Towards a practical tool for online monitoring of solid oxide fuel cell operation: an experimental study and application of advanced data analysis approaches. Appl Energy 2018;222:748–61. https://doi.org/10.1016/j.apenergy.2018.03.182.
[9] Wei J, Osipova T, Malzbender J, Krüger M. Mechanical characterization of SOFC/SOEC cells. Ceram Int 2018;44:11094–100. https://doi.org/10.1016/j.ceramint.2018.03.103.
[10] Nguyen XV, Chang CT, jung GB, Chan SH, Lee WT, Chnag SW, Kao IC. Study of sealants for SOFC. Int J Hydrogen Energy 2016;41:21812–9. https://doi.org/10.1016/j.ijhydene.2016.07.156.
[11] Salvo M, Casalegno V, Rizzo S, Smeacetto F, Ventrella A, Ferraris M. Glasses and glass-ceramics as brazing materials for high temperature applications. In: Sekulić dušan P, editor. Woodhead Publishing series in Welding and other joining technologies, Advances in Brazing. 17. Woodhead Publishing; 2013. p. 525–44. https://doi.org/10.1533/9780857096500.3.525.
[12] Smeacetto F, Salvo M, Santarelli M, Leone P, Ortigoza-Villalba GA, Lanzini A, Ajitdoss LC, Ferraris M. Performance

of a glass-ceramic sealant in a SOFC short stack. Int J Hydrogen Energy 2013;38:588–96.

[13] Malzbender J, Zhao Y, Beck T. Fracture and creep of glass-ceramic solid oxide fuel cell sealant materials. J Power Sources 2014;246:574–80. https://doi.org/10.1016/j.jpowsour.2013.08.010.

[14] Gross SM, Federmann D, Remmel J, Pap M. Reinforced composite sealants for solid oxide fuel cell applications. J Power Sources 2011;196:7338–42. https://doi.org/10.1016/j.jpowsour.2011.02.002.

[15] Fakouri Hasanabadi M, Malzbender J, Groß-Barsnick SM, Abdoli H, Kokabi AH. Finite element optimization of sample geometry for measuring the torsional shear strength of glass/metal joints. Ceram Int 2020;46:4857–63. https://doi.org/10.1016/j.ceramint.2019.10.221.

[16] Fakouri Hasanabadi M, Malzbender J, Groß-Barsnick SM, Abdoli H, Kokabi AH, Faghihi-Sani MA. Micro.scale evolution of mechanical properties of glass-ceramic sealant for solid oxide fuel/electrolysis cells, cream. Bar Int 2021;47:3884–91. https://doi.org/10.1016/j.ceramint.2020.09.250.

[17] Elsayed H, Javed H, Sabato AG, Smeacetto F, Bernardo E. Novel glass-ceramic SOFC sealants from glass powders and reactive silicone binder. J Eur Ceram Soc 2018;38:4245–51. https://doi.org/10.1016/j.jeurceramsoc.2018.05.024.

[18] Smeacetto F, Salvo M, D'Hérin Bytner FD, Leone P, Ferraris M. New glass and glass-ceramic sealants for planar solid oxide fuel cells. J Eur Ceram Soc 2010;30:933–40. https://doi.org/10.1016/j.jeurceramsoc.2009.09.033.

[19] Krainova DA, Saetova NS, Kuzmin AV, Raskovalov AA, Eremin VA, Ananyev MV, Steinberger-Wilckens R. Non-crystallising glass sealants for SOFC: effect of Y_2O_3 addition. Ceram Int 2020;46:5193–200. https://doi.org/10.1016/j.ceramint.2019.10.266.

[20] Dev B, Walter ME, Arkenberg GB, Swartz SL. Mechanical and thermal characterization of ceramic/glass composite seal for solid oxide fuel cells. J Power Sources 2014;245:958–66. https://doi.org/10.1016/j.jpowsour.2013.07.054.

[21] Timurkutluk B, Altan T, Celik S, Timurkutluk C, Palaci Y. Glass fiber reinforced sealants for solid oxide fuel cells. Int J Hydrogen Energy 2019;44:18308–18. https://doi.org/10.1016/j.ijhydene.2019.05.116.

[22] Wang SF, Hsu YF, Cheng CS, Hsieh YC. SiO2-Al2O3-Y2O3-ZnO glass sealants for intermediate temperature solid oxide fuel cell applications. Int J Hydrogen Energy 2018;38:14779–90. https://doi.org/10.1016/j.ijhydene.2013.09.034.

[23] Malzbender J. Curvature and stresses for bi-layer functional ceramic materials. J Eur Ceram Soc 2010;30:3407–13. https://doi.org/10.1016/j.jeurceramsoc.2010.07.036.

[24] Rangel-Hernández VH, Fang Q, Babelot C, Lohoff R, Blum L. An experimental investigation of fracture processes in glass-ceramic sealant by means of acoustic emission. Int J Hydrogen Energy 2020;45:27539–50. https://doi.org/10.1016/j.ijhydene.2020.07.031.

[25] Gross-Barsnick S-M, Babelot C, Federmann D, Pabst U. Optimization of tensile strength measurements on glass-ceramic sealant used for SOFC stacks. ECS Trans 2015;68:2573–82. https://doi.org/10.1149/06801.2573ecst.

[26] Smeacetto F, Salvo M, Ferraris M, Casalegno V, Asinari P, Chrysanthou A. Characterization and performance of glass–ceramic sealant to join metallic interconnects to YSZ and anode-supported-electrolyte in planar SOFCs. J Eur Ceram Soc 2008;28:2521–7. https://doi.org/10.1016/j.jeurceramsoc.2008.03.035.

[27] Wei J, Pećanac G, Malzbender J. Mechanical behavior of silver reinforced glass–ceramic sealants for solid oxide fuel cells. Ceram Int 2015;41:15122–7. https://doi.org/10.1016/j.ceramint.2015.08.084.

[28] Ventrella A, Salvo M, Avalle M, Ferraris M. Comparison of shear strength tests on AV119 epoxy-joined ceramics. J Mater Sci 2010;45:4401–5.

[29] Ferraris M, de la Pierre S, Sabato AG, Smeacetto F, Javed H, Walter C, Malzbender J. Torsional shear strength behavior of advanced glass-ceramic sealants for SOFC/SOEC applications. J Eur Ceram 2020;40:4067–75.

[30] Fakouri Hasanabadi M, Kokabi AH, Faghihi-Sani MA, Groß-Barsnick SM, Malzbender J. Room- and high-temperature torsional shear strength of solid oxide fuel/electrolysis cell sealing material. Ceram Int 2019;45:2219–25. https://doi.org/10.1016/j.ceramint.2018.10.134.

[31] Osipova T, Wei J, Pecanac G, Malzbender J. Room and elevated temperature shear strength of sealants for solid oxide fuel cells. Ceram Int 2016;42:12932–6. https://doi.org/10.1016/j.ceramint.2016.05.064.

[32] Stephens EV, Vetrano JS, Koeppel BJ, Chou Y, Khaleel MA. Experimental characterization of glass-ceramic seal properties and their constitutive implementation in solid oxide fuel cell stack models. J Power Sources 2009;193:625–31. https://doi.org/10.1016/j.jpowsour.2009.02.080.

[33] Abdoli H, Alizadeh P, Boccaccini D, Agersted K. Effects of thermal aging on thermo-mechanical behavior of a glass sealant for solid oxide cell applications. J Eur Ceram 2014;34:2525–34.

[34] Mousa Mirabid H, Nemati A, Faghihi-Sani MA, Fakouri Hasanabadi M. Effect of YSZ sol-gel coating on interaction of Crofer22 APU with sealing glass for solid oxide fuel/electrolysis cell. J Alloys Compd 2020;847:156496. https://doi.org/10.1016/j.jallcom.2020.156496.

[35] Sabato AG, Rost A, Schilm J, Kusnezoff M, Salvo M, Chrysanthou A, Smeacetto F. Effect of electric load and dual atmosphere on the properties of an alkali containing diopside-based glass sealant for solid oxide cells. J Power Sources 2019;415:15–24. https://doi.org/10.1016/j.jpowsour.2019.01.051.

[36] Sabato AG, Cempura G, Montinaro D, Chrysanthou A, Salvo M, Bernardo E, Secco M, Smeacetto F. Glass ceramic sealant for solid oxide fuel cells application: characterization and performance in dual atmosphere. J Power Sources 2016;328:262–70. https://doi.org/10.1016/j.jpowsour.2016.08.010.

[37] Malzbender J, Steinbrech RW. Advanced measurement techniques to characterize thermo-mechanical aspects of solid oxide fuel cells. J Power Sources 2007;173:60–7. https://doi.org/10.1016/j.jpowsour.2007.07.072.

[38] Xiang Yu, Da Yule, Zheng Zhong, Shikazono Naoki, Jiao Zhenjun. Thermomechanical stress analysis of solid oxide fuel cell anode based on three-dimensional microstructure reconstruction. Int J Hydrogen Energy 2020;45:19791–800. https://doi.org/10.1016/j.ijhydene.2020.05.121.

[39] Asnt. Acoustic emission testing. Nondestructive testing handbook. 3rd ed., vol. 6; 2005. USA.

[40] Hellier CJ. Chapter 10: acoustic emission testing. In: Handbook of nondestructive evaluation. McGraw-Hill; 2001.

[41] Miller RK, Findlay RD, Carlos MF. Acoustic emission testing. In: K. H. EV, Miller POMRK, editors. NDT handbook; 2005. p. 122–46. Columbus.

[42] Zhou W, Shang Yj, Zhang P, Yin H, Ma L. Statistical analysis of acoustic emission signals and tensile deformation measurement for three dimensional carbon fiber braided composites. SN Appl Sci 2020;2:1237. https://doi.org/10.1007/s42452-020-3069-5.

[43] Mukhopadhyay CK, Jayakumar T, Raj B, Venugopal S. Statistical analysis of acoustic emission signals generated during turning of a metal matrix composite. J Braz Soc Mech Sci & Eng 2012;2:145–54.

[44] Sause M, Hamstad M. 7.14 acoustic emission analysis. In: Beaumont PWR, Zweben CH, editors. Comprehensive composite materials II; 2018. https://doi.org/10.1016/B978-0-12-803581-8.10036-0. 291-236.

[45] M.G.R. Sause. In situ monitoring of fiber-reinforced composites: theory, basic concepts, methods and applications. Springer Int. Publishing. Switzerland. Doi: 10.1007/978-3-319-30954-5.

[46] Sato K, Omura K, Hashida T, Yashiro K, Yugami H, Kawada T, Mizusaki J. Tracking the onset of damage mechanism in ceria-based solid oxide fuel cells under simulated operating conditions. J Test Eval 2006;34:246–50. https://doi.org/10.1520/JTE12707.

[47] Surgeon M, Vanswijgenhoven E, Wevers M, Van der Biest O. Acoustic emission during tensile testing of SiC-fibre-reinforced BMAS glass-ceramic composites. Composites Part A 28A 1997;96:473–80.

[48] Scholey JJ, Wilcox PD, Wisnom Mr MR, Friswell MI. Quantitative experimental measurements of matrix cracking and delamination using acoustic emission. Composites Part A Appl Sci manuf 2010;41:612–23. https://doi.org/10.1016/j.compositesa.2010.01.008.

[49] Nozawa T, Ohsone R, Tanigawa H. Characterization of torsion fracture behavior of F82H HIP joints with damage monitoring by acoustic emission. Fusion Eng Des 2017;124:985–9. https://doi.org/10.1016/j.fusengdes.2017.05.134.

[50] Hu Yuting, Li Shuncai, Li Daquan, Vadim Slatin. Yield criteria and strenght conditions considering comprehensive mechanical and acoustic emission characteristics of tension-torsion composite deformation of nylon materials. Compos Struct 2020;243:112278. https://doi.org/10.1016/j.compstruct.2020.112278.

[51] Hao Wenfeng, Yuan Zengrui, Teng Can, Zhang Lu, Zhao Guoqi, Luos Ying. Acoustic emission monitoring of damage progression in 3D braiding composite shafts torsional tests. Compos Struct 2019;208:141–9.

[52] Greven BC. Glass-ceramic sealant reinforcement for high-temperature applications. PhD. Thesis. Forschungszentrum Jülich. Germany: Jülich; 2015. ISBN: 978-3-95806-042-5.

[53] Gross SM, Koppitz T, Remmel J, Bouche JB, Reisgen U. Joining properties of a composite glass-ceramic sealant. Fuel Cell Bull 2006;9:12–5. https://doi.org/10.1016/S1464-285(06)71320-7.

[54] Brendt J, Gross SM, Babelot C, Natour G. The influence of ZnO and V2O5 on the crystallization behavior of BaO-CaO-SiO2 glass ceramic sealants. J Non Cryst Solids 2018;501:78–84. https://doi.org/10.1016/j.jnoncrysol.2018.01.032.

[55] Cela B, Sillapawatana S, Gross SM, Koppitz T, Conradt R. Influence of filler additives on the effective viscosity of glass-ceramic composite sealants. J Univ Chem Technol Metall 2012;47:449–58. http://dl.uctm.edu/journal/node/j2012-4/14_BeatrizCela_449-458.pdf.

[56] Fakouri Hasanabadi M, Faghihi-Sani MA, Kokabi AH, Malzbender J. The analysis of torsional shear strength test of sealants for solid oxide fuel cells. Ceram Int 2017;43:12546–50. https://doi.org/10.1016/j.ceramint.2017.06.128.

[57] Patent US 10 , 170 , 775 B2.

[58] Vallen Systeme GmbH. 2017.

[59] Sause MGR. Investigation of pencil-lead breaks as acoustic emission sources. J Acoust Emiss 2011;29:184–96.

[60] Origin(Pro), Version. Northampton, MA, USA: OriginLab Corporation; 2020.

[61] Li Shenhou, Hu Kangjia, Hui Wenchang, Cai Yangyang, Zhang Yong. Shear strength and interfacial characterization of borosilicate glass-to-metal seals. J Alloys Compd 2020;827:154275. https://doi.org/10.1016/j.jallcom.2020.154275.

[62] Wiederhorn SM. Fracture of ceramics. In: Watchman Jr JB, editor. Mechanical and thermal properties of ceramics, vol. 303. NBS Special Publication; 1969. p. 217–42.

[63] Liens A, Reveron H, Douillard T, Blanchard N, Lughi V, Sergo V, Laquai R, Müller BR, Bruno G, Schomer S, Fürderer T, Adolfsson E, Courtois N, Swain M, Chevalier J. Phase transformation induces plasticity with negligible damage in ceria-stabilized zirconia-based ceramics. Acta Mater 2020;183:261–73. https://doi.org/10.1016/j.actamat.2019.10.046.

[64] Gostautas RS, Ramirez G, Peterman RJ, Meggers D. Acoustic emission monitoring and analysis of glass fiber-reinforced composites bridge decks. J Bridge Eng 2005;10:713–21.

[65] Gholizadeh S, Leman Z, Baharudin BTHT. A review of the application of acoustic emission technique in engineering. Struct Eng Mech 2015;54:1075–95. https://doi.org/10.12989/sem.2015.54.6.1075.

[66] Oskouei AR, Heidary H, Ahmadi M, Farajpur M. Unsupervised acoustic emission data clustering for the analysis of damage mechanisms in glass/polyester composites. Mater Des 2012;37:416–22. https://doi.org/10.1016/j.matdes.2012.01.018.

[67] Haselbach W, Lauke B. Acoustic emission of debonding between fiber and matrix to evaluate local adhesion. Compos Sci Technol 2003;63:2155–62. https://doi.org/10.1016/S0266-3538(03)00193-3.

[68] Marec A, Thomas JH, Guerjoma R. Damage characterization of polymer-based composite materials: multivariable analysis and wavelet transform for clustering acoustic emission data. Mech Syst Signal Process 2008;22:1441–64. https://doi.org/10.1016/j.ymssp.2007.11.029.